FREE SURFACE EFFECT ON THE HYDRODYNAMICS OF AN UNDERWATER VEHICLE HULLFORM, THE DARPA SUBOFF

Reference NO. IJME732, DOI No: 10.5750/ijme.v164i1.732

X W Ling, Z Q Leong, C K H Chin, M D Woodward, Australian Maritime College, Australia.

KEY DATES: Submitted: 15/05/21; Final acceptance: 23/05/22; Published 15/06/22

SUMMARY

This paper presents the numerical study on the hydrodynamic coefficients of the submarine hull form "DARPA SUBOFF" when deeply submerged and near the free surface when travelling straight ahead and at a range of drift angles. The Computational Fluid Dynamics (CFD)-based numerical model was validated with experimental data existing in the public domain for the SUBOFF, travelling over a range of drift angles when deeply submerged at a constant speed and in a straight line near the free surface over a range of speeds. The free surface effect on the hydrodynamic behaviour of the SUBOFF was then investigated throughout a range of speeds, drift angles and submergence depths. Results show that the effects of the free surface diminish rapidly with submergence and the near free surface hydrodynamic behaviour of the SUBOFF is highly Froude number dependent.

NOMENCLATURE

A_S	Surface area (m^2)
C_D	Refer to X'
C_P	Pressure coefficient (-); $(P-P_\infty) / 0.5\rho U$
D	Diameter (m)
D^*	Submergence depth (-)
Fn	Froude number (-); $U / \sqrt{(g\,L)}$
g	Acceleration due to gravity (m s^{-2})
h	Distance from centreline of the SUBOFF to the calm free surface (m)
L	Length (m)
M	Pitch moment (N m)
M'	Pitch moment coefficient (-); $M / (0.5\rho U^2 L^3)$
N	Yaw moment (Nm)
N'	Yaw moment coefficient (-); $N / (0.5\rho U^2 L^3)$
P	Pressure (Pa)
P_∞	Free-stream pressure (Pa)
R_G	Convergence ratio
Re	Reynolds number (-)
U	Velocity of body centre of buoyancy relative to fluid (m s^{-1})
X	Longitudinal / Surge force (N)
X'	Longitudinal / Surge force coefficient (-); $X / (0.5\rho U^2 L^2)$
X_{CB}	Longitudinal centre of buoyancy (m)
Y	Transverse / Sway force (N)
Y'	Transverse / Sway force coefficient; $Y / (0.5\rho U^2 L^2)$
x, y, z	Cartesian coordinates in the x, y, z-direction (m)
Z	Heave force (N)
Z'	Heave force coefficient (-); $Z / (0.5\rho U^2 L^2)$
β	Drift angle (°)
$\varepsilon_{III-II} / \varepsilon_{II-I}$	Difference in measured forces / moments between subsequent mesh refinements
ρ	Fluid density (kg m^{-3})
λ	Wavelength (m)
μ	Fluid dynamic viscosity (kg m^{-1} s^{-1})

1. INTRODUCTION

Underwater vehicles (UV) such as diesel-electric powered submarines are periodically required to operate at periscope depth for snorting or other mission specific purposes such as littoral operation and communication. This shallow submergence depth induces free surface interactions that can alter the flow field surrounding the hull. The first and most apparent effect of an UV travelling near the free surface is the generation of surface wakes, much like the wake of a surface vessel. These surface waves are the result of the interaction between the pressure field distribution over the hull and the free surface. A UV travelling along a straight line with a constant velocity generates a wave system similar to that of the classic Kelvin wake pattern of a surface ship. The Kelvin wake can be said to be one of the most thoroughly studied surface wave due to its regular structure and it can be used as an indicator in detection for an underwater object's state of motion. In addition, the energy required to generate surface waves can adversely affect the hydrodynamics of the vessel. With a decrease in submergence depth (i.e., a shallowly submerged vessel), it is expected that the drag of the body will increase as the amplitude of the surface waves increase. In a shallowly submerged flow regime, the free surface significantly alters the pressure distribution along the hull and therefore the hydrodynamic forces and moments on the body. Underwater vehicles are usually tested for deep water where the resistance, other forces and moments are viscous-dominant where wave-making and wave-induced forces are ignored or are negligible. The motion close to the free surface usually takes place when sailing in areas of limited depth which further complicates the situation. Hence, the manoeuvring qualities of the vessel changes due to the following

factors: wave-making on the longitudinal force and moment but also on the transverse force and moment, caused by drift angle and the angular velocity of the vessel.

The free surface's presence and its subsequent influence on underwater vehicles has been the subject of numerous studies long before the advent of the modern-day diesel and nuclear submarines. The first of which was conducted by Havelock who calculated the drag increase due to the free surface for various geometry including a sphere, oblate and prolate spheroids, and ellipsoids travelling at small submergence depths (Havelock, 1917, Havelock, 1931a, Havelock, 1931b). It was shown that the drag component due to the presence of the free surface exhibited an oscillatory behaviour with respect to Froude number and that this effect diminishes rapidly with an increase in submergence depth. This behaviour is more commonly known now as wave making resistance and is attributed to the energy expended by the vehicle when generating waves as in the case of any surface vessel. For an underwater vehicle however, there is an extra component to consider which is the submergence depth. As shown by Crook (1994) with a slender axisymmetric body travelling at zero incidence and in proximity with the free surface also experiences a vertical heave force and a pitching moment which all vary with Froude number.

Wilson-Haffenden (2009) at the Australian Maritime College (AMC) investigated both experimentally and numerically a bare hull SUBOFF in straight-ahead motion near the free surface. This study focused on various submergence depths ranging from 1.1 to 5.5 times the depth-to-diameter ratio (defined later on as submergence depth, D^*) and a Froude number range from 0.13 to 0.64. The experimental data gained is used in this thesis for verification whereas the numerical results allow for comparisons between CFD solver methods. The year after this, a degree of complexity was added to both the experimental and numerical setup by Van Steel (2010) via the addition of a sail as well as modelling the sting support used in the experiment. It was noted that modelling the sting produced results which matched experimental data much more closely albeit underpredicting slightly, but it was deemed inconclusive as there were only a limited number of simulations run with a sting. Additionally, the numerical simulations could not capture the oscillatory behaviour of drag with respect to Froude number after the first drag peak. As shown later, using current CFD techniques, the hump and hollow behaviour of drag that is expected of a body travelling near the free surface can be captured with accuracy. Neulist (2011) followed up on Van Steel's experiments with a smaller but denser range of submergence depths and additionally measured the vertical forces and moments acting on the SUBOFF. Consideration was also put into the selection of the artificial turbulence stimulator with experimental runs conducted to determine the optimal Hama strip thickness. The experimental work focused mainly on the experimental set-up to ensure accurate measurements. This involved measuring the vibration and inclination of the test rig and by careful selection of the load cells used. These (Wilson-Haffenden, 2009, Van Steel, 2010, Neulist, 2011) research projects make up the near free surface experiments at the AMC that investigate the hydrodynamic behaviour of a shallowly submerged SUBOFF geometry. All the aforementioned studies have been on underwater vehicles travelling near the free surface at zero incidence. It can be said that as opposed to underwater vehicles travelling at zero incidence, there is a lack of investigation that evaluate the free surface effects of an underwater vehicle at nonzero incidence in both the vertical and horizontal plane.

Hence, the main objective of this paper is to evaluate and quantify the effects of the free surface on the hydrodynamics of an underwater vehicle. This will first include a mesh independence study, whereby the sensitivity of the numerical results is first investigated and then can be deemed mesh independent. Next involves validation against experimental results for a deeply submerged SUBOFF undergoing steady drift motion and for a SUBOFF undergoing straight ahead motion when near the free surface. This is then extended to numerical simulations which involve changing the submergence depth, drift angle and Froude number of the SUBOFF to obtain the hydrodynamic coefficients with respect to all three aforementioned variables. The simulations are conducted using the Baseline Reynolds Stress Model (BSLRSM) using the commercial code ANSYS Fluent. In modelling the free surface, the volume of fluid (VOF) is used. The generic underwater vehicle used throughout this study is the DARPA SUBOFF, this generic underwater vehicle has been used in various experimental studies which form the basis of validating the numerical model used throughout this paper. Thus, this paper focuses on the following: an investigation into the accuracy of CFD in predicting hydrodynamic forces and moments acting on an underwater vehicle near the free surface and the development of a CFD model which allows numerical model tests to be conducted.

2. STEADY DRIFT ANGLE EXPERIMENTAL VALIDATION

This section examines the ability of Computational Fluid Dynamics (CFD) to reproduce the experimentally measured forces and moments acting on the unappended SUBOFF undergoing steady drift motion by Roddy (1990). The simulations were performed with the commercial CFD code ANSYS Fluent using the Reynolds-averaged Navier-Stokes (RANS) scheme with the Baseline Reynolds Stress Model (BSLRSM) turbulence model in a pseudo-transient state. The advantages of BSLRSM over other popular turbulence models has been previously studied (Leong et al., 2012) and in summary, the accuracy gained outweighs the increased computational time compared to other RANS-based turbulence models.

2.1 GEOMETRY MODEL

An axisymmetric SUBOFF hull with the particulars presented in Table 1 was used for the steady drift angle validation study. The origin of the body-fixed coordinate frame coincides with the longitudinal centre of buoyancy, X_{CB} of the SUBOFF, located at 0.462L from the nose. The coordinate system used is a standard right-handed coordinate system with positive x pointing forward, positive y to port and positive z pointing downwards away from the free surface.

Table 1: Geometric characteristics of the SUBOFF in Roddy (1990), Wilson-Haffenden (2009) and Neulist (2011); and Joubert BB2 in Dawson (2014).

Description	Roddy (1990)	Wilson-Haffenden (2009) & Neulist (2011)	Dawson (2014)
Length, L [m]	4.356	1.556	1.955
Diameter, D [m]	0.508	0.181	0.230
Surface area, A_S [m^2]	5.986	0.779	1.238

2.2 SIMULATION SETUP

The computational domain was modelled with similar dimensions as that of the David Taylor Research Centre (DTRC) Towing Basin to ensure likeness when validating CFD results with the experimental data by Roddy (1990). The dimensions and test parameters are listed in Table 2. The boundary conditions are as such: the SUBOFF hull as a no-slip wall, the top, sides and bottom as free-slip walls, the upstream boundary as a pressure inlet and the downstream boundary as a pressure outlet. The domain extends approximately three body lengths (3L) upstream, five body lengths (5L) downstream and three and a half body lengths (3.5L) on both sides.

Table 2: Steady drift angle domain dimensions.

Description	Symbol	Value	Unit
Basin width	-	15.545	[m]
Basin depth	-	6.706	[m]
Model depth	h	3.353	[m]
Towing velocity	U	3.344	[m s^{-1}]
Reynolds number	Re	14.16×10^6	[-]
Drift angle	β	0 to 18	[°]
Fluid density	ρ	9.983×10^2	[kg m^{-3}]
Fluid dynamic viscosity	μ	1.028×10^{-3}	[kg m^{-1} s^{-1}]

2.3 GRID INDEPENDENCE STUDY

A drift angle of 18°, the maximum angle presented in the experimental dataset was selected for the mesh independence study. Figure 1 shows the percentage difference of predicted forces and moments from the finest 11.4 million mesh elements as a function of mesh element density. At about 5.5 million elements, the predictions were within 3% of the finest mesh investigated. As a conservative measure, the 5.7 million element mesh was used instead.

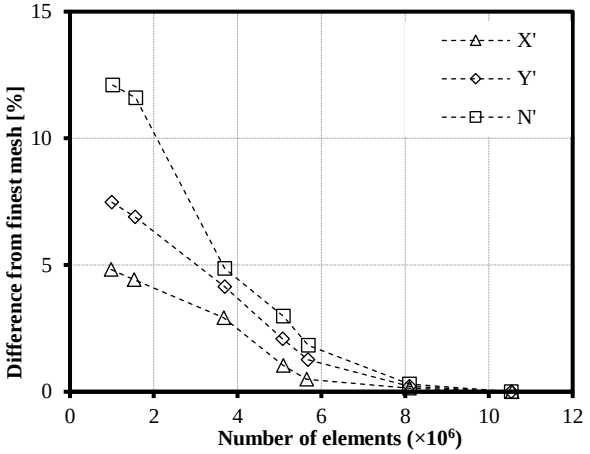

Figure 1: Percentage difference of the surge coefficient X', sway coefficient Y', and yaw coefficient N' predictions to the finest 11.4 million element mesh solution for the various number of mesh elements simulated for the SUBOFF at a drift angle, β of 18°.

Table 3: Percentage difference between the 3 finest meshes with Richardson extrapolation.

% change	X'	Y'	N'
III	1.875	1.316	0.567
II	0.338	0.268	0.213
I (Finest)	0.038	0.055	0.080

To further verify that the numerical model is mesh independent, Richardson extrapolation (Richardson, 1911, Celik & Karatekin, 1997) was conducted with the 3 finest meshes of 5.7, 8.1, and 10.5 million elements (from Figure 1). This gives a refinement factor of approximately 1.4 between each of the meshes. Additionally, based on the changes of the forces/moments between each of the mesh configurations, the convergence ratio which is the difference in measured forces/moments between subsequent mesh refinements is calculated, i.e., between 5.7 to 8.1 million (grids III and II), and between 8.1 to 10.5 million (grid II and I). This is represented as follows: $R_G = \varepsilon_{III\text{-}II} / \varepsilon_{II\text{-}I}$, where $\varepsilon_{III\text{-}II}$ is the difference in the force/moment between grids III and II, and $\varepsilon_{II\text{-}I}$ is the difference in the force/moment between grids II and I. The calculated values for convergence ratio, R_G show monotonic convergence (Eça & Hoekstra, 2009). Finally, the Richardson extrapolation value was then calculated and the percentage difference between the three finest meshes to the extrapolated value is as shown in Table 3. It again shows that the numerical model is indeed mesh independent, with the percentage difference between the 5.7 million element mesh (Grid III in Table 3) and the Richardson extrapolation value being 1.875% for X', 1.316% for Y', and 0.567% for N'.

2.4 EXPERIMENTAL COMPARISON

Figure 3 shows the predicted surge force, sway force, and yaw respectively on the SUBOFF undergoing steady drift

motion in comparison with the experiments conducted at DTRC (Roddy, 1990). The experiments were conducted for a deeply submerged SUBOFF at a Froude number, *Fn* of 0.512 over a drift angle range of $0° \leq \beta \leq 18°$. The predictions were found to be in good agreement with the positive angle data set of experimental measurements and a previous study by Leong et al. (2012) shows similar agreement. The experimental measurements were reported with an uncertainty of 10% although it does not include the contribution from the mounting structure. Poor repeatability is shown between the positive and negative drift angles of the experimental results. This was attributed to the resolution of the load cells used which were reported to be inadequate for the measurement of small forces (a coefficient of 1.0×10^{-3} or a force of about 100 N). The term submergence depth, D^* is a depth-to-diameter ratio where the depth is the distance between the calm water level and the centreline of the SUBOFF, denoted as *h*. The term is defined as $D^* = h / D$. To ensure that the numerical model can accurately predict the hydrodynamic forces acting on a deeply submerged SUBOFF even in the presence of a free surface, the verification study was conducted on a SUBOFF when deeply submerged (a submergence depth, D^* of 6.6).

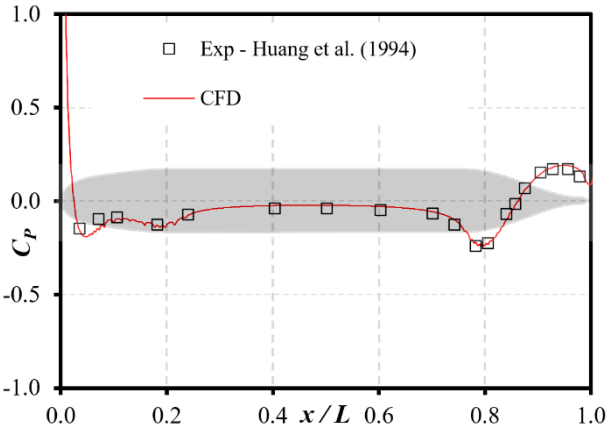

Figure 2: Pressure distribution along the length of a deeply submerged SUBOFF at *Fn* = 0.462.

In addition, the pressure coefficient on the surface of the SUBOFF also formed part of the validation. In Figure 2 the pressure coefficient, C_P is shown for a deeply submerged SUBOFF (at 6.6D^*) at a Froude number, *Fn* of 0.462. The results are in good agreement with Huang et al. (1994) who adopted a point above the model at x/D = 7.3. This validation study considered a reference point of 15*D* and the simulated domain is sufficiently wide to avoid blockage effects altogether. Additional comparisons (though not shown in Figure 2) were made with other CFD results from Gorski et al. (1990) and Posa and Balaras (2016) being in close agreement with experimental results from Huang et al. (1994).

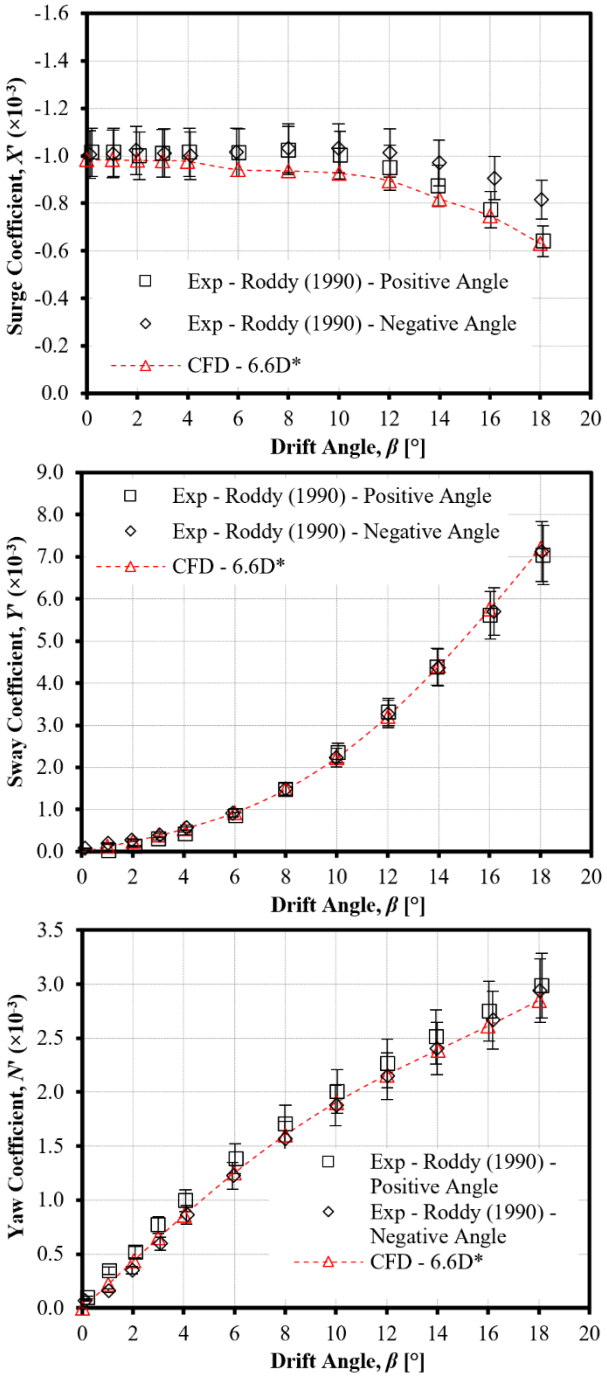

Figure 3: CFD predictions and experimental measurements from Roddy (1990) of the surge coefficient, X' (Top); sway coefficient, Y' (Middle); and yaw coefficient, N' (Bottom) vs drift angle, β.

3. STRAIGHT-AHEAD NEAR FREE SURFACE EXPERIMENTAL VALIDATION

This section examines the ability of CFD to reproduce the experimentally measured forces and moments acting on the unappended SUBOFF undergoing straight-ahead motion when near the free surface by Wilson-Haffenden (2009), Neulist (2011), and Dawson (2014). The drag coefficient, heave coefficient and pitch coefficient were compared over the presented experimental Froude number range ($0.13 \leq Fn \leq 0.65$) and submergence depth range ($1.1 \leq D^* \leq 6.6$). Several experimental comparisons were required as certain datasets only include drag coefficient and not heave and pitch coefficient which are expected to be more sensitive to the free surface.

3.1 SIMULATION SETUP

An axisymmetric SUBOFF hull with the particulars presented in Table 1as well as comparisons for a Joubert BB2 hull was used for the straight-ahead near free surface validation study. The dimensions for the domain in this section of this study were matched to that of the AMC towing tank with dimensions as such: a width of 3.55m and standard water depth of 1.50 m. Similar to the steady drift angle validation study, the numerical model was prescribed similar boundary conditions.

Figure 4 shows the mesh model of the SUBOFF near free surface case. A hex-dominant mesh was used as the cells (mesh elements) are aligned to the Cartesian coordinate system of the domain and these cells can be said to be less skewed as the cells are not stretched or compressed which is important for capturing the free surface. The free surface mesh was sized according to the recommendations from CD-Adapco (in Spence, 2014) and ITTC (2011) as in Table 4. Because the free surface profile (the Kelvin wake pattern) is of interest, around 140 cells per wavelength was used.

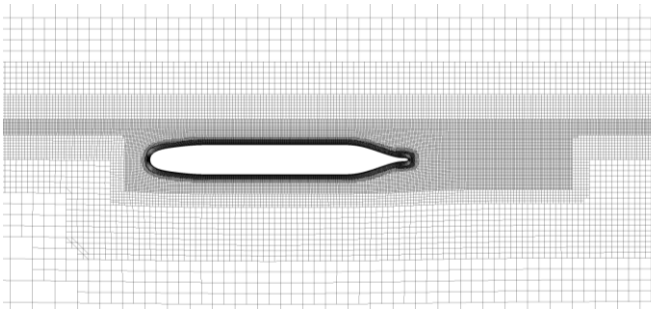

Figure 4: Mesh model for a near free surface SUBOFF.

Table 4: Mesh recommendations for surface waves.

Description	Cells per wavelength	Cells per amplitude
CD-Adapco	80 to 100	20
ITTC	40	10

3.2 EXPERIMENTAL COMPARISON

Before discussing experimental results, note that the experimental datasets from Wilson Haffenden (2009) and Neulist (2011) have been corrected for sting effects and so comparisons are being made with a "bare hull" experimental SUBOFF. The first experimental dataset in Figure 5 is from Wilson-Haffenden (2009) where a bare hull SUBOFF was investigated. Results show that CFD is able to capture free surface effects, namely the hump and hollow behaviour of drag coefficient. The second experimental data in Figure 6 from Neulist (2011) shows much better agreement even though at a much larger submergence depth. The variances in experimental datasets can also be seen when comparing Neulist (2011) to Wilson-Haffenden (2009) where even though similar geometry and submergence depth were used in both experiments, the drag coefficient in Wilson-Haffenden (2009) is significantly higher.

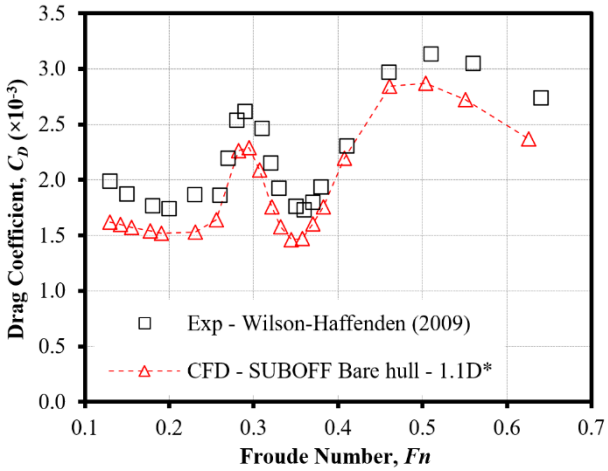

Figure 5: CFD predictions and experimental measurements of the drag coefficient, C_D at a submergence depth, D^* of 1.1 from Wilson-Haffenden (2009).

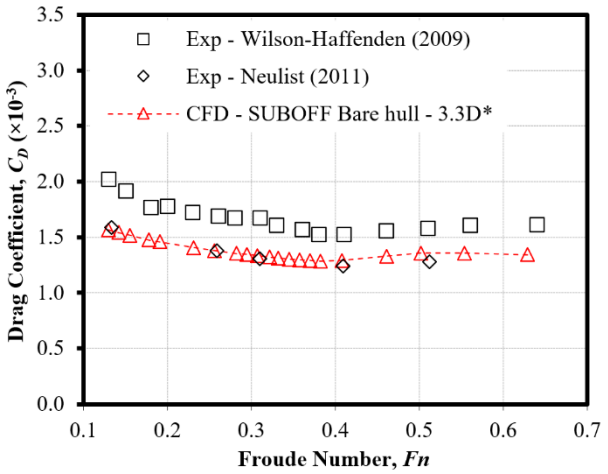

Figure 6: CFD predictions and experimental measurements of the drag coefficient, C_D at a submergence depth, D^* of 3.3 from Wilson-Haffenden (2009) and Neulist (2011).

Next, the dataset presented from Dawson (2014) in Figure 7 uses the BB2 Joubert hull which has a slightly different hull form, with L/D of 8.50 compared to the SUBOFF with L/D of 8.57. The non-dimensionalisation of this dataset is also slightly different as such. For example, drag coefficient, $C_D = X / (0.5\rho U^2 S)$, and pitch coefficient, $M' = M / (0.5\rho U^2 SL)$. Even though the geometries are different and so likeness cannot be ensured, having anot her experimental dataset of an underwater vehicle near the free surface still proves invaluable in assessing the fidelity of the numerical model, especially in the vertical plane, where experimental data for a bare hull underwater vehicle geometry is not available. Note that this dataset has not been corrected for sting effects and so the experimental drag coefficient is slightly lower due to the sting affecting aft region pressure recovery, thus reducing experimental drag predictions.

To conclude the validation sections, based on sections 3 and 4, it has been shown quite clearly that the numerical model is able to replicate experimental force and moment recordings from Roddy (1990), with respect to drift angle, being capable of resolving separated flow at high drift angles. Pressure coefficient on the SUBOFF's surface was also shown to be accurate compared to Huang et al's (1994) experiment in Figure 2. As for near free surface experiments, CFD has also been shown to be capable of clearly capturing the trends for drag, heave and pitch which exhibit a hump and hollow behaviour when near the free surface.

4. NEAR FREE SURFACE EFFECTS

4.1 EFFECTS OF SUBMERGENCE DEPTH, D^*

The increase in drag of the SUBOFF as it approaches the free surface can be attributed to two flow mechanisms: (1) an increase in local flow velocity between the free surface and the stern region as submergence depth decreases (flow constriction at the stern, i.e., venturi effect where there is a change in the pressure distribution along the length of the SUBOFF and (2) an increase in wave making resistance as submergence depth decreases. Figure 9 shows that as submergence depth, D^* increases the free surface elevations generated by the SUBOFF (from this section on with a length of 4.356 m) diminish rapidly until almost indiscernible wave amplitudes at $4.4D^*$. The wavelength stays consistent with respect to submergence depth at around 0.8 body lengths at all submergence depths investigated. The increase in hydrodynamic forces as the underwater vehicle approaches the free surface is due to wave-making resistance, the most apparent of which is the increase in drag force with a decrease in submergence depth. Additionally, the increase in hydrodynamic forces of a shallowly submerged underwater vehicle can be attributed to the free surface's effect on the pressure distribution around the vehicle's body. The crests and troughs of a shallowly submerged underwater vehicle modifies the pressure field around the underwater vehicle's hull, creating localised regions of high and low pressure. Figure 8 shows the velocity contour sampled about the centreline plane of the SUBOFF at a submergence depth of $1.1D^*$ and a Froude number of 0.512 and a close-up of the stern region. Here, the effect of fluid constriction as the SUBOFF approaches the free surface can be clearly seen with fast water flow just above the aft shoulder region where water is shallowest due to the occurrence of a wave trough.

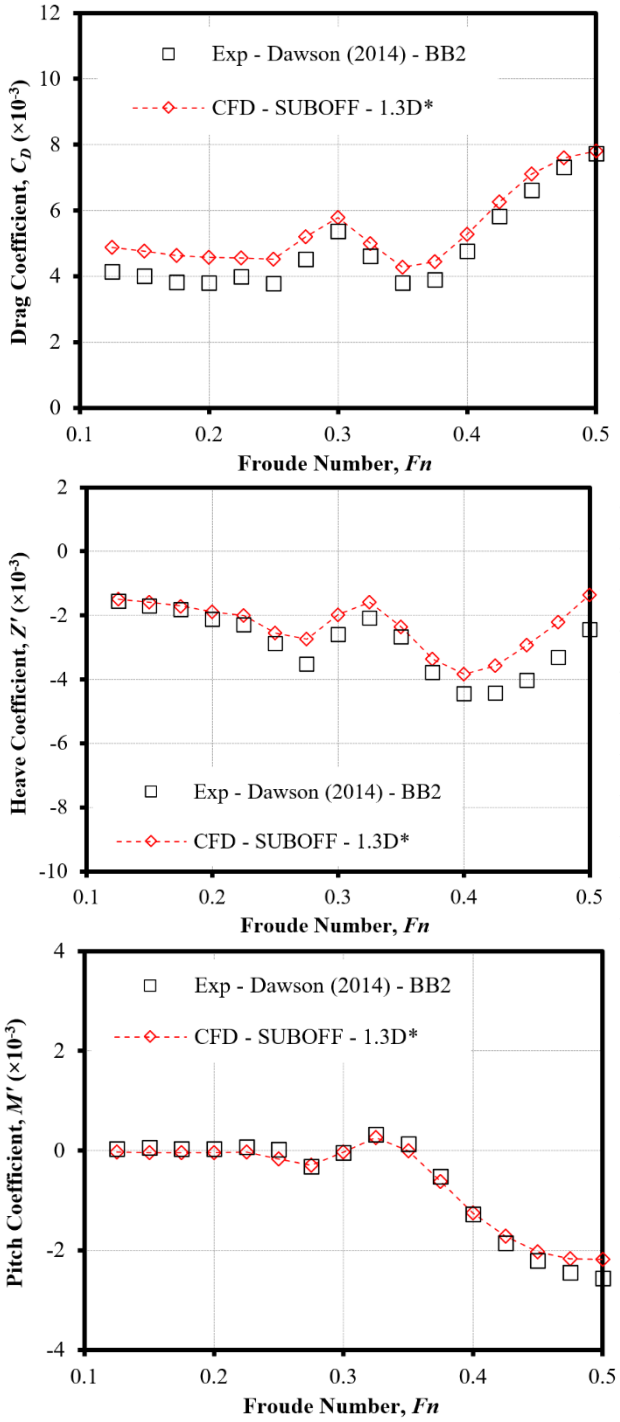

Figure 7: CFD predictions and experimental measurements of the drag coefficient, C_D (Top), heave coefficient, Z' (Middle), and pitch coefficient, M' (Bottom) at a submergence depth, D^* from Dawson (2014) of a BB2 Joubert hull.

The main wave components of the SUBOFF are:

1. The bow wave system (with a high pressure at entry that starts with a crest),

2. The aft shoulder system (due to low pressure at midships and higher pressure at stern),

3. The stern wave system (due to rising pressure gradients and decreasing velocity, starting with a trough).

The first and third wave components will occur at fixed places (i.e., the nose and the stern) whilst the second component is dependent on the form of the aft shoulder. In the case of the SUBOFF, the aft shoulder wave system occurs at a longitudinal position, x/L of approximately 0.80 (x of 1.5 m in Figure 9 or for better clarity in Figure 11 accompanied by the large decrease in C_P). These wave systems move forwards with ship speed and hence, wave phases are dependent on speed. As speed increases, the length of the bow wave increases, until it coincides and interferes with the stern wave. As a result of this interference, the resistance curve of the SUBOFF that approaches the free surface exhibits an oscillatory nature with speed (meaning that they exhibit humps and hollows as in Figure 10).

Figure 10 shows a hump and hollow oscillatory behaviour in both maximum free surface elevation and drag coefficient with respect to Froude number, most pronounced at submergence depths of 1.1D* and 1.3D* with the behaviour diminishing rapidly even at 2.2D*. This effect can be explained by considering the bow and stern wave systems. The transverse waves generated at the bow travel aft relative to the SUBOFF and when they reach the stern-generated waves, they interact. If the crests of the two wave systems coincide, the resultant wave is of a greater amplitude; likewise, if the crest of one coincides with the trough of another, the resultant energy and hence amplitude will be less. As the vehicle's speed (Froude number) increases, the wavelengths of the wave systems increase and so there are times when crests combine and other times when crest and trough coincide. When the wave system is in phase (when the two wave systems constructively interact), the hump occurs whilst the hollow occurs when the wave system is out of phase (when they cancel each other out). The reinforcement or cancellation of wave systems (the increase or decrease in maximum free surface elevation) is associated with an increase or decrease in the drag coefficient (Newman, 1977, van Manen and van Oossanen, 1988, Molland et al., 2011, Birk, 2019).

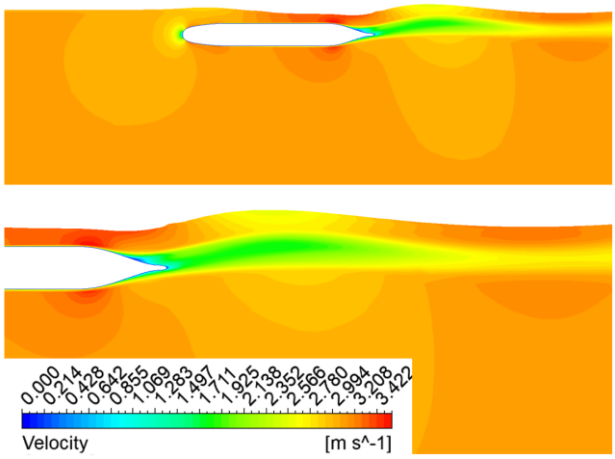

Figure 8: Velocity contour at a submergence depth, D* of 1.1 at a Froude number, Fn of 0.512 (Top) and close-up of the stern section (Bottom) sampled about centreline plane.

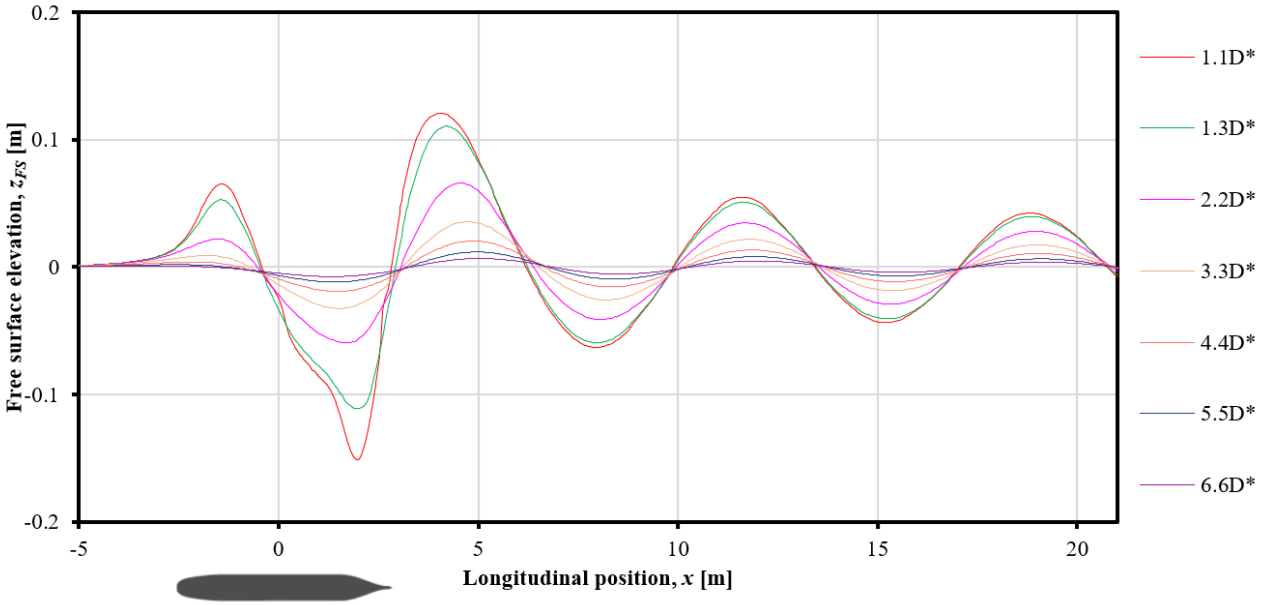

Figure 9: Free surface elevations, z_{FS} vs longitudinal position, x at various D* sampled about the y = 0 plane at Fn = 0.512 (For reference, X_{CB} of SUBOFF is at x = 0 with a D* of 1.1 corresponding to 0.5588 m from the origin).

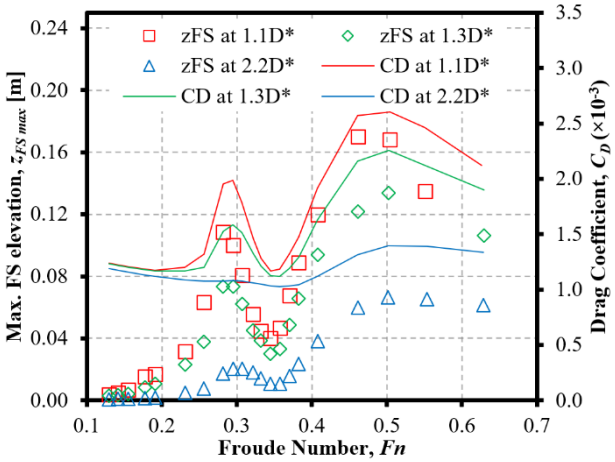

Figure 10: Maximum free surface elevation, z_{FSmax} and drag coefficient, C_D vs Froude number, *Fn* at submergence depths, *D** of 1.1, 1.3 and 2.2 respectively from top to bottom (solid lines represent drag coefficient and square points represent maximum free surface elevation).

Figure 11 shows the free surface elevations and pressure distribution along the length of the SUBOFF. When *Fn* = 0.295, the free surface elevation is higher, and this is due to the bow wave crest coinciding with the stern wave crest. Constructive interference occurs resulting in a high free surface elevation value. As *Fn* increases, the normalised bow wavelength, λ/L increases and the bow wave crest starts moving away from the stern wave crest, resulting in gradually lower free surface elevations as the crests of the two wave systems move out of phase from one another. At *Fn* = 0.357, the normalised bow wavelength, λ/L is 0.80 and the bow wave crest is approximately at the aft shoulder trough (located at $\lambda/L \approx 0.80$). Destructive interference occurs and this can be seen from the lower free surface elevation as well as the hollow in both drag coefficient and maximum free surface elevation in Figure 11.

Figure 12 shows the top-down view of the Kelvin wake pattern generated by the SUBOFF at a submergence depth of 1.1*D** and at Froude numbers of 0.295 and 0.357. Again, as was shown in Figure 10 the free surface elevation is significantly lower at a Froude number of 0.357 where destructive interference occurs between the bow wave and the aft shoulder wave. Additionally, from Figure 12, it can be seen that at higher speeds, the waves are spaced much further apart whereas when at low speeds, the wave spacing is much narrower.

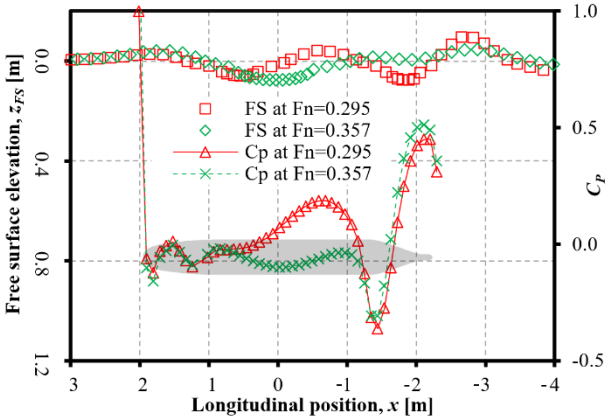

Figure 11: Centreline free surface elevations, z_{FS} and pressure distribution, C_P along the length of a SUBOFF at a submergence depth, *D** of 1.1 at Froude numbers, *Fn* of 0.295 and 0.357. Note that the SUBOFF is only shown for length scale for pressure distribution.

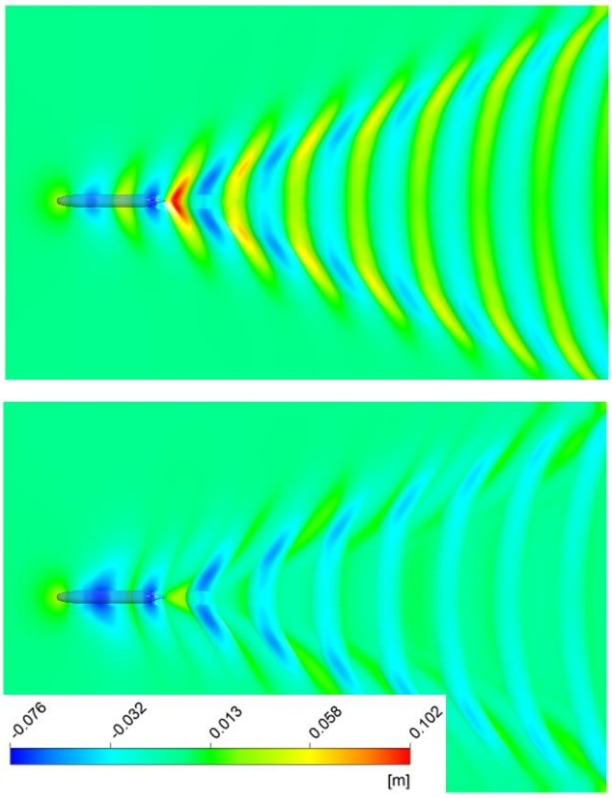

Figure 12: Free surface elevations, z_{FS} at a submergence depth, *D** of 1.1 at Froude numbers, *Fn* of 0.295 (Top) and 0.357 (Bottom).

Figure 13 shows the drag coefficient of the SUBOFF (with a length of 4.489m) over a range of speeds and submergence depths. The distinct hump and hollow behaviour of drag for a UV near the free surface can be seen. A clear decrease in free surface effect with increasing submergence depth can be seen whereby drag values at 3.3D* are almost at deeply submerged where flow is unaffected by a boundary. This is most evident in the hump that occurs between $0.25 \leq Fn \leq 0.35$. Similar to free surface elevations staying consistent in their wavelength in Figure 9, the general trend of drag coefficient should similarly be consistent as well as one is the product of another.

Figure 14 shows the heave force whereby a positive heave force is indicative of bodily rise, whereby the SUBOFF experiences suction towards the free surface. At higher Froude numbers of 0.5 or more, the directionality of the heave force tends towards the opposite direction, meaning that the SUBOFF is instead repelled from the free surface. This sudden change in suction and repulsion combined with the effects of pitching moment changing direction may cause manoeuvrability issues. Again, as submergence depth increases, the effects of the free surface diminish rapidly until the SUBOFF experiences no free surface suction or repulsion (a heave force coefficient of zero).

Pitching moment, shown in Figure 15 oscillates between a nose-up and nose-down moment. A positive pitching moment indicates a nose-down moment whereas a negative pitch indicates a nose-up moment. The changes in pitching moment are highly correlated with the pressure field surrounding the hull which varies with submergence depth and speed. Similar to drag, pitching moment decreases rapidly with submergence depth and approaches deeply submerged values at depths of more than 3.3D*. At 3.3D*, pitch behaves very similarly to that of a deeply submerged SUBOFF at 6.6D* indicating that the Fn range that is of most interest is smaller than 3.3D* or even 2.2D*.

Based on recommendations made in near free surface work by Neulist (2011), additional simulations will be run at smaller intervals for submergence depths of 1.1 to 2.2 as this is the region where the free surface's effects are expected to be the most significant. The same can also be said for the next section for drift angles.

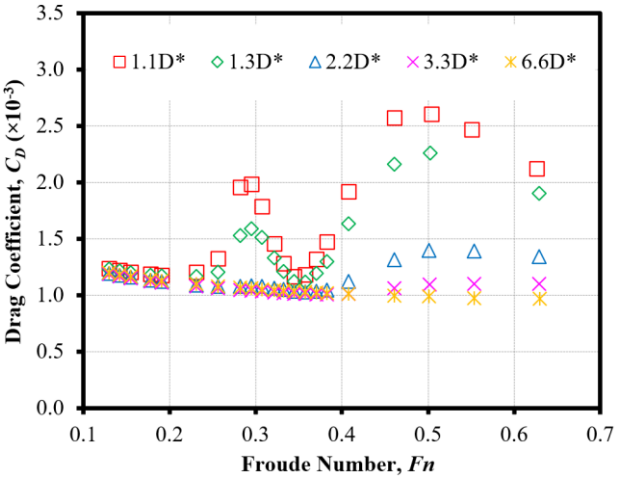

Figure 13: Drag coefficient, C_D vs Froude number, Fn at various submergence depths, D*.

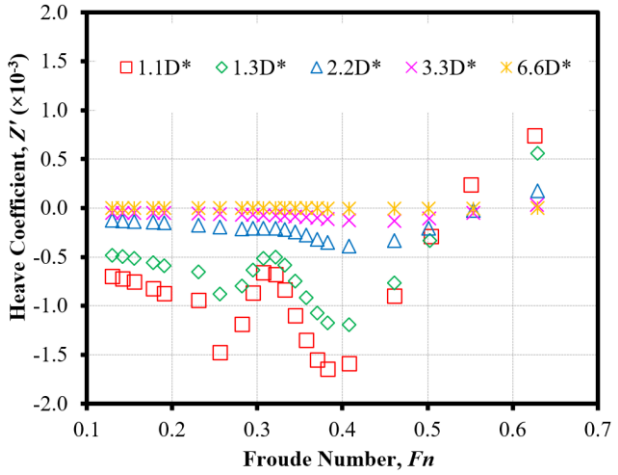

Figure 14: Heave coefficient, Z' vs Froude number, Fn at various submergence depths, D*.

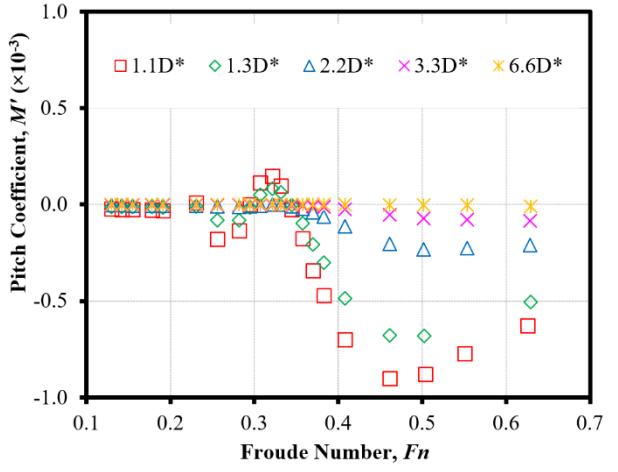

Figure 15: Pitch coefficient, M' vs Froude number, Fn at various submergence depths, D*.

4.2 EFFECTS OF DRIFT ANGLE, β

Figures 16, and 17 show the surge coefficient, X', and the sway coefficient, Y'. As the underwater vehicle approaches the free surface, there is a significant increase in both X' and Y' due to wave making resistance. When shallowly submerged, an increase in lateral velocity, v (defined as $v = U \sin \beta$) causes an increase in X'. Conversely, when deeply submerged at $6.6D^*$ an increase in lateral velocity, however, leads to a decrease in X'. Over the entire range of submergence depths, Y' increases with respect to drift angle due to the increase in pressure differential between the sides of the hull. As for N', the trend stays consistent with respect to submergence depth but is simply decreased. The surge force, X can be interpreted as resistance due to the longitudinal velocity component, u (defined as $u = U \cos \beta$) in the x-direction. When an underwater vehicle is fully submerged, a reduction in u (an increase in v at increasing drift angles) gives rise to a reduction in resistance acting in the x-direction. When shallowly submerged, the effects of wave making resistance can be clearly identified in X' as the underwater vehicle approaches the free surface. In short, when shallowly submerged, an increase in lateral velocity, v leads to an increase in surge force, X when the converse is true for a deeply submerged underwater vehicle.

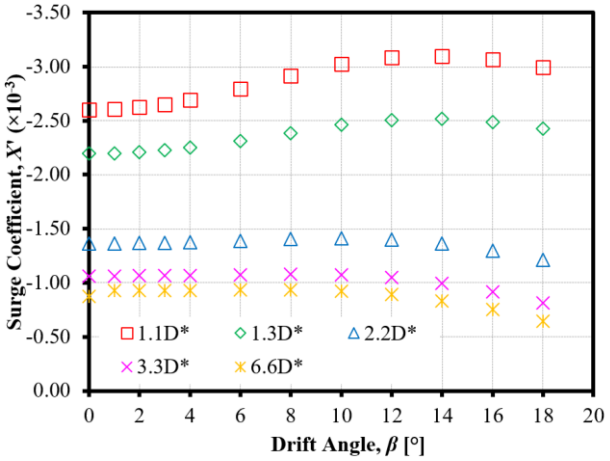

Figure 16: Surge coefficient, X' vs drift angle, β at various submergence depths, D^*.

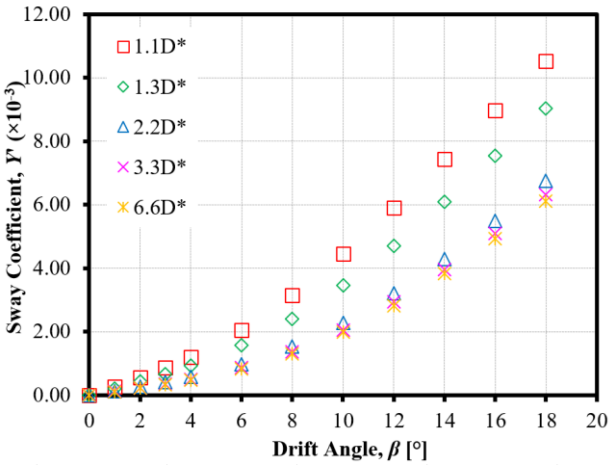

Figure 17: Sway coefficient, Y' vs drift angle, β at various submergence depths, D^*.

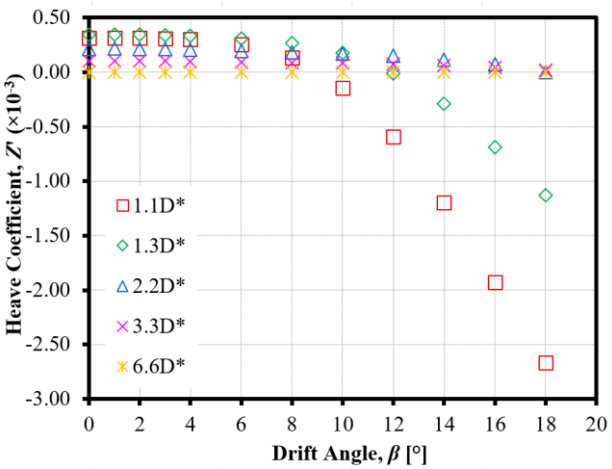

Figure 18: Heave coefficient, Z' vs drift angle, β at various submergence depths, D^*.

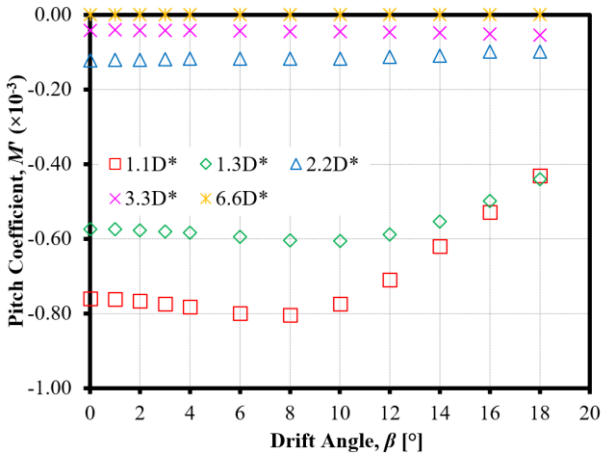

Figure 19: Pitch coefficient, M' vs drift angle, β at various submergence depths, D^*.

An increase in surge force, X with respect to lateral velocity, v is due to an increase in energy imparted by the underwater vehicle to elevate the free surface which gives rise to an increase in wave making resistance. Figure 20 shows the maximum free surface elevation with respect to drift angle, β over a range of submergence depths. Maximum free surface elevations increase with respect to both drift angle and submergence depth even though overall speed remains constant at a Froude number, Fn of 0.512. This increase in free surface elevation is likely due to the effect of vortical flow where a drop in the dynamic pressure at the core of the vortex causes larger depressions of the free surface above it (shown with a black arrow in Figure 21). As lateral velocity increases with drift angle, the vortical flow structure grows and further reduces the dynamic pressure resulting in larger free surface depressions. This free surface depression causes a large X-force due to the increase in wave making resistance.

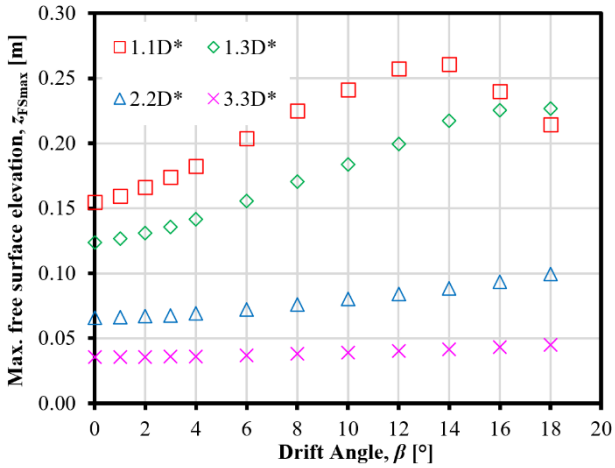

Figure 20: Maximum free surface elevation, z_{FSmax} vs drift angle, β at various submergence depths, D*.

Figure 22 shows the axial vortices shed by the SUBOFF at a drift angle of 18° over a range of submergence depths from submergence depths of 1.1D*, 1.3D* and 2.2D*. Along the length of the SUBOFF, crossflow separation grows stronger moving towards the stern. From the closeup of the vortex, the free surface's effect on the vertical forces and moments can be seen whereby the top vortex is drawn towards the free surface, giving rise to a heave force (which grows stronger with drift angle as in Figure 18) and pitching moment (which is also affected as in Figure 19). The influence of the free surface diminishes with submergence depth and that at a submergence depth of 2.2D* the top and bottom vortices are almost symmetrical.

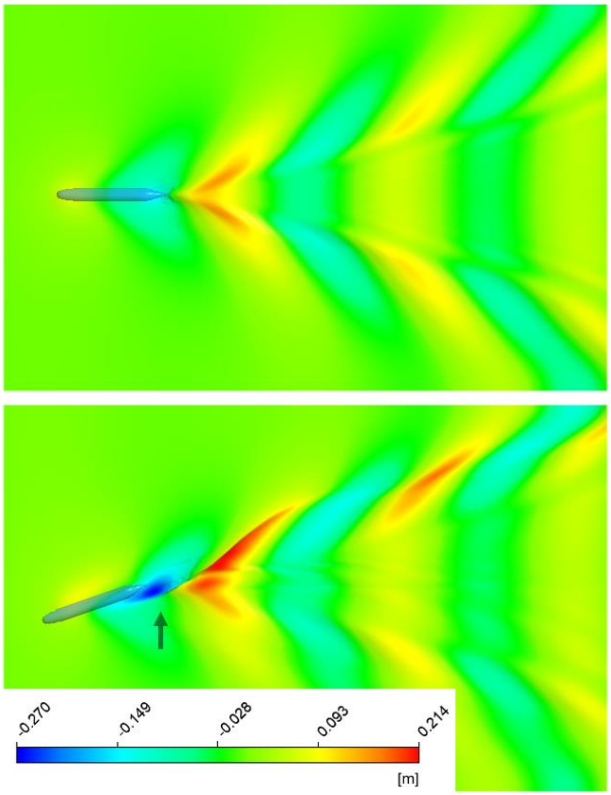

Figure 21: Free surface elevation at a submergence depth, D* of 1.1, Froude number, Fn of 0.512 at drift angles, β of 0° (Top) and 18° (Bottom).

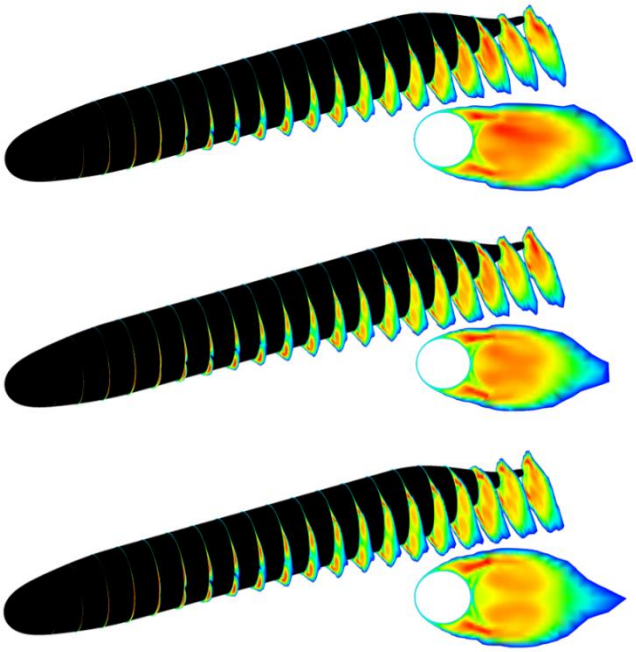

Figure 22: Axial vortices shedding from the SUBOFF undergoing steady drift motion at submergence depths, D* of 1.1 (Top), 1.3 (Middle), and 2.2 (Bottom). Close-up shows the 3rd axial vortex from the stern.

Sway force, Y originates from the pressure differential between the sides of the SUBOFF when at an angle of drift and can be thought of as the resisting force exerted on the SUBOFF in the y-direction. The yaw moment, N is the moment generated by the Y-force about the z-axis. Figure 23 shows the pressure coefficient of a deeply submerged SUBOFF at an axial plane 1 m aft of X_{CB} for drift angles of 0° and 18°. A growing pressure differential exists with increasing drift angle. This growing pressure differential is the cause for the increase in Y-force with respect to sway velocity, v. Crossflow separation grows stronger between the two sides of the SUBOFF, and the vortex core of the leeward vortex can be clearly identified from the dark blue circles.

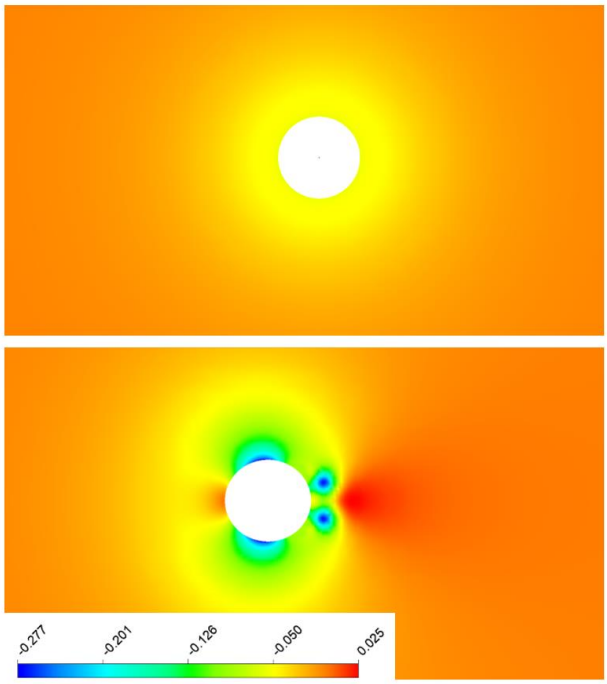

Figure 23: Pressure coefficient, C_P of a deeply submerged SUBOFF at a Froude number, Fn of 0.512 at drift angles, β of 0° (Top) and 18° (Bottom). Note that the sampling plane is an yz plane at x = 1 m aft of X_{CB}.

From Figure 24, at a submergence depth of 1.1D*, there is a much larger low-pressure region in the stern region of the SUBOFF compared to 2.2D*. There is also a large drop in pressure at the stern and this could be attributed to the rapid stern taper of the SUBOFF. This departure of the low-pressure region from the body when shallowly submerged indicates that the vortex downstream of the aft shoulder does not remain attached to the SUBOFF. Overall, the increased pressure differential between the two sides of the SUBOFF is further exacerbated by the presence of the free surface, causing an increase in Y' with respect to submergence depth (Figure 17).

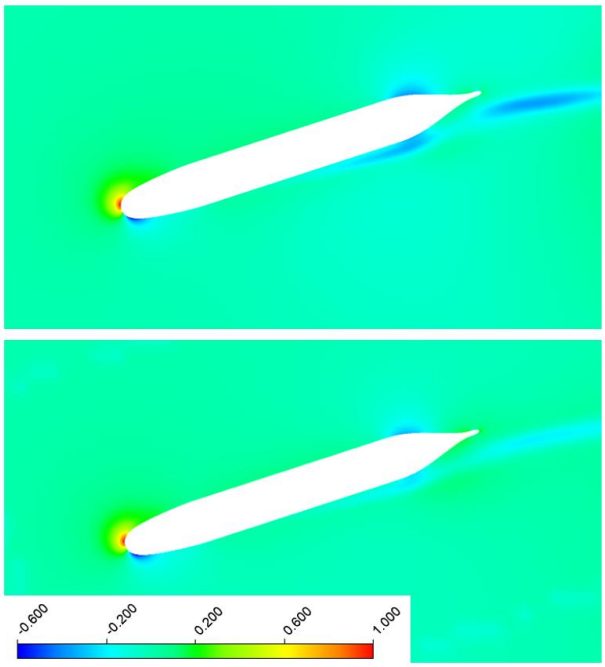

Figure 24: Pressure coefficient, C_P at a drift angle, β of 18° and Froude number, Fn of 0.512 at a submergence depth, D* of 1.1 (Top) and 2.2 (Bottom). Note that the sampling plane is an xy plane with z at centreline plane of the SUBOFF.

5. CONCLUSION

Simulations of a SUBOFF axisymmetric hull were conducted with two objectives: to determine the effects of the free surface on the hydrodynamic coefficients and also to determine the distance from the free surface at which its effects become insignificant. The fidelity of the numerical model was validated using experimental results of the SUBOFF undergoing straight-ahead motion when near the free surface, steady drift when deeply submerged and the pressure coefficient on the SUBOFF's body.

Results show that the free surface induces large effects on the hydrodynamic coefficients of the SUBOFF and that the free surface's effects diminish rapidly with distance and can be said to be insignificant at non-dimensionalised distances of 3 or more with respect to hull diameter. Additionally, in investigating the effects of the free surface, the aft shoulder of the SUBOFF was determined to be the area of largest significance as the largest free surface depression occurs at an x/L of 0.8, leading to large vertical forces and moments.

Future work involves extending the current simulation test matrix from two-dimensional lines of hydrodynamic coefficient vs. Froude number to a three-dimensional surface describing the hydrodynamic coefficient with respect to both submergence depth, D* and Froude number, Fn. This method will also be extended to other variables such as drift angle and pitch angle in combination with Froude number. Additionally, experimental investigations should be conducted on a near

free surface bare hull SUBOFF to provide heave and pitch measurements for the validation of CFD simulations as there is a lack of available data on the effects of the free surface on the vertical plane coefficients of a bare hull SUBOFF.

Regression analysis is also expected to be conducted and aims to describe these three-dimensional surface contours as functions of their variables, giving an output equation. For example, describing drag coefficient as a function of both submergence depth and Froude number; or describing drag coefficient as a function of both drift angle and Froude number. This process however involves a significant number of data points, which might not be feasible given computational resource constraints and hence, optimization needs to be conducted to determine the number of data points required for accurate regression analysis and the methods used to describe the trends when data points are sparser (i.e., the interpolation methods, trendline type, or polynomial order).

6. REFERENCES

1. BIRK, L. (2019). *Fundamentals of Ship Hydrodynamics: Fluid Mechanics, Ship Resistance and Propulsion*, School of Naval Architecture and Marine Engineering, University of New Orleans, New Orleans, LA, United States, John Wiley & Sons. https://www.academia.edu/40043158/Fundamentals_of_Ship_Hydrodynamics (Accessed 15th May 2021)
2. CELIK, I.B., & KARATEKIN, O. (1997). *Numerical Experiments on Application of Richardson Extrapolation With Nonuniform Grids*. Journal of Fluids Engineering – Transactions of the ASME, 119, 584-590. https://citeseerx.ist.psu.edu/viewdoc/download?doi=10.1.1.1091.1742&rep=rep1&type=pdf (Accessed 24th Feb 2022)
3. CROOK, T. P. (1994). *An Initial Assessment of Free Surface Effects on Submerged Bodies*. Masters of Science in Mechanical Engineering Thesis, Naval Postgraduate School, Monterey, California. https://apps.dtic.mil/dtic/tr/fulltext/u2/a288546.pdf (Accessed 15th May 2021)
4. ECA, L. & HOEKSTRA, M. (2009). *Evaluation of numerical error estimation based on grid refinement studies with the method of the manufactured solutions*, Computers & Fluids, 38 (8), 1580-1591. http://ftp.demec.ufpr.br/CFD/bibliografia/erros_numericos/Eca_Hoekstra_2009.pdf (Accessed 24th Feb 2022)
5. GORSKI, J. J., COLEMAN, R. M. & HAUSSLING, H. J. (1990). *Computation of Incompressible Flow Around the DARPA SUBOFF Bodies*. Bethesda, Maryland 20084-5000: David Taylor Research Center. https://apps.dtic.mil/dtic/tr/fulltext/u2/a226481.pdf (Accessed 15th May 2021)
6. HUANG, T. T., LIU, H.-L., GROVES, N. C., FORLINI, T. J., BLANTON, J. N. & GOWING, S. (1994). *Measurements of Flows Over an Axisymmetric Body with Various Appendages (DARPA SUBOFF Experiments)*. 19th Symposium on Naval Hydrodynamics, Washington DC, USA. National Academy Press, 321-346.
7. HAVELOCK, T. H. (1917). *Some cases of wave motion due to a submerged obstacle*. Proceedings of the Royal Society of London, Series A, Containing Papers of a Mathematical and Physical Character, London. The Royal Society Publishing. https://royalsocietypublishing.org/doi/10.1098/rspa.1917.0036 (Accessed 15th May 2021)
8. HAVELOCK, T. H. (1931a). *The wave resistance of a spheroid*. Proceedings of the Royal Society of London, Series A, Containing Papers of a Mathematical and Physical Character, London. https://royalsocietypublishing.org/doi/10.1098/rspa.1931.0052 (Accessed 15th May 2021)
9. HAVELOCK, T. H. (1931b). *The wave resistance of an ellipsoid*. Proceedings of the Royal Society of London, Series A, Containing Papers of a Mathematical and Physical Character, London. https://royalsocietypublishing.org/doi/10.1098/rspa.1931.0113 (Accessed 15th May 2021)
10. HUONG, Y. T. (2018). *Numerical Analysis on the Effect of Submergence Depth on the Bare-Hull Model Scaled BB2 at AMC Towing Tank*. Bachelor of Engineering (Naval Architecture) (Honours) Thesis, Australian Maritime College, Newnham, Tasmania.
11. ITTC (2011). *Practical Guidelines for Ship CFD Applications.* 26th ITTC Specialist Committee on CFD in Marine Hydrodynamics. International Towing Tank Conference. https://ittc.info/media/1357/75-03-02-03.pdf (Accessed 15th May 2021)

12. JIMENEZ, J. M., HULTMARK, M. & SMITS, A. J. (2010). *The intermediate wake of a body of revolution at high Reynolds numbers.* Journal of Fluid Mechanics, 659, 516-539. https://www.cambridge.org/core/journals/journal-of-fluid-mechanics/article/intermediate-wake-of-a-body-of-revolution-at-high-reynolds-numbers/6CD525A4521BE0A088AFE765010A7315 (Accessed 15th May 2021)
13. LEONG, Z., RAMUTHUGALA, D., PENESIS, I. & NGUYEN, H. (2012). *RANS-based CFD Prediction of the Hydrodynamic Coefficients of DARPA SUBOFF Geometry in Straight-Line and Rotating Arm Manoeuvres.* International Journal of Maritime Engineering, 154.
14. MACKAY, M. (1993). *A Review of Sting Support Interference and Some Related Issues for the Marine Dynamic Test Facility (MDTF).* Defence Research Establishment Atlantic: National Defence Research and Development Branch, Dartmouth, Nova Scotia. https://apps.dtic.mil/dtic/tr/fulltext/u2/a271806.pdf (Accessed 15th May 2021)
15. MOLLAND, A. F., TURNOCK, S. R. & HUDSON, D. A. (2011). *Ship Resistance and Propulsion: Practical Estimation of Ship Propulsive Power*. Cambridge, Great Britain, Cambridge University Press. https://eprints.soton.ac.uk/188555/ (Accessed 15th May 2021)
16. NEULIST, D. (2011). *Experimental Investigation into the Hydrodynamic Characteristic of a Submarine Operating Near the Free Surface*. Bachelor of Engineering (Naval Architecture), Australian Maritime College.
17. NEWMAN, J. N. (1977). *Marine Hydrodynamics.* The Massachusetts Institute of Technology. Cambridge, Massachusetts.
18. POSA, A. & BALARAS, E. (2016). *A numerical investigation of the wake of an axisymmetric body with appendages*. Journal of Fluid Mechanics, 792, 470-498. https://www.cambridge.org/core/journals/journal-of-fluid-mechanics/article/a-numerical-investigation-of-the-wake-of-an-axisymmetric-body-with-appendages/71B03615EE98884A6B8B98E3B3C1991A (Accessed 15th May 2021)
19. RICHARDSON, L. F., (1991) *The Approximate Arithmetical Solution by Finite Differences of Physical Problems Involving Differential Equations, with an Application to the Stresses in a Masonry Dam*. Philosophical Transactions of the Royal Society of London Series, 210, 307–357. https://www.jstor.org/stable/90994?origin=ads (Accessed 24th Feb 2022)
20. RODDY, R. F. (1990). *Investigation of the Stability and Control Characteristics of Several Configurations of the DARPA SUBOFF Model (DTRC Model 5470) from Captive-Model Experiments*. Bethesda, Maryland 20084-5000: David Taylor Research Center. https://apps.dtic.mil/dtic/tr/fulltext/u2/a227715.pdf (Accessed 15th May 2021)
21. SPENCE, S. 2014. *Numerical Investigation of Free Surface Flows*, Norwegian University of Science and Technology, Department of Marine Technology, Trondheim, Norway. https://www.semanticscholar.org/paper/Numerical-Investigation-of-Free-Surface-Flows-Spence/4acfedc150cf6f010cd1b070816272d0497d8b33 (Accessed 15th May 2021)
22. VAN MANEN, J. D. & VAN OOSSANEN, P. (1988). *Resistance*. In: LEWIS, E. V. (ed.) *Principles of Naval Architecture*. 601 Pavonia Avenue, Jersey City, NJ: The Society of Naval Architects and Marine Engineers.
23. VAN STEEL, S. (2010). *Investigation into the effect of wave making on a submarine approaching the surface*. Bachelor of Engineering (Naval Architecture) (Honours) Thesis, Australian Maritime College, Newnham, Tasmania.
24. WILSON-HAFFENDEN, S. (2009). An *Investigation into the Wave Making Resistance of a Submarine Travelling Below the Free Surface*. Bachelor of Engineering (Naval Architecture) (Honours) Thesis, Australian Maritime College, Newnham, Tasmania.

